Near field development of artificially generated high Reynolds number turbulent boundary layers

Eduardo Rodríguez-López, Paul J.K. Bruce and Oliver R.H. Buxton

May 18, 2016

Abstract

Particle image velocimetry (PIV) is conducted in the near field of two distinct wall-mounted trips for the artificial generation of a high Reynolds number turbulent boundary layer. The first of these trips consists of high aspect ratio obstacles which are supposed to minimize the influence of their wakes on the near-wall region, contrasting with low aspect ratio trips which would enhance this influence. A comprehensive study involving flow description, turbulent/non-turbulent interface detection, a low order model description of the flow and an exploration of the influence of the wake in the near-wall region is conducted and two different mechanisms are clearly identified and described. First, high aspect ratio trips generate a *wall-driven* mechanism whose characteristics are: a thinner, sharper and less tortuous turbulent/non-turbulent interface and a reduced influence of the trips' wake in the near-wall region. Second, low aspect ratio trips generate a *wake-driven* mechanisms in which their turbulent/non-turbulent interface is thicker, less sharply defined and with a higher tortuosity and the detached wake of the obstacles presents a significant influence on the near-wall region. Study of the low order modelling of the flow field suggests that these two mechanisms may not be exclusive to the particular geometries tested in the present study but, on the contrary, can be explained based on the predominant flow features. In particular, the distinction of these two mechanisms can explain some of the trends that have appeared in the literature in the past decades.

1 Introduction

Tripping conditions in turbulent boundary layers (TBL) for wind tunnel testing has been the basis for several studies in the past decades. Broadly, they can be classified in two groups depending on whether their aim is to generate an artificial high Reynolds number (Re) TBL or, alternatively, to promote the transition from an earlier laminar state. A considerable number of the studies belonging to the former

group follow the work proposed by Armitt and Counihan (1968); Counihan (1969). However, there have been other attempts at high Re flow generation in the past; without trying to provide an exhaustive review of the different methods one can cite, for instance, Nagib et al. (1976); Cook (1978); Arie et al. (1981); Davidson et al. (1996); Kornilov and Boiko (2012) amongst many others. For a deeper review of the different methods the reader is referred, for instance, to Hunt and Fernholz (1975). Special mention is required for Klebanoff and Diehl (1951), who studied different trips in order to increase boundary layer thickness for a given downstream position, paying special attention to recover the canonical properties of the boundary layer downstream of an adaptation region.

Considering studies in which the aim is to study the evolution of standard turbulent boundary layers (not artificially generated to simulate an extraordinary high Re), a considerable effort has been invested into understanding the effects of different trips to trigger transition from an earlier laminar state to a turbulent one. However, as pointed out by Marusic et al. (2010) and Schlatter and Örlü (2012), on many occasions the exact tripping conditions for different experiments are not adequately described, which may lead to difficulty when comparing results with previously published data. Two studies deserve special attention with regards to the tripping effects on the downstream development of the TBL; both Erm and Joubert (1991) (experimental) and Schlatter and Örlü (2012) (computational) concluded that, *for the tested trips' geometry and location*, a self-similar state (independent of the trip employed) is obtained at about $Re_\theta > 2000$, where Re_θ is the Reynolds number based on the momentum thickness, θ, the freestream velocity, U_∞, and the kinematic viscosity, ν. This result seemed contradictory with the study of Castillo and Johansson (2002) who reported that the trip dependency was maintained up to the last station measured ($Re_\theta > 5000$). Recently, Marusic et al. (2015) used large trips to deliberately *over-trip* the TBL (horizontal threaded bars of 6 and 10 mm) and studied their evolution with the downstream coordinate. They concluded that far enough from the trip, the canonical properties of the boundary layer were recovered even for the most disturbed case.

Although contradictory at first sight, all these studies arrive to a similar conclusion. After a trip (independently of whether it is employed to artificially thicken a turbulent boundary layer or to force transition from a laminar state) there is an adaptation region and, far enough downstream, the trip is forgotten and the canonical properties of the TBL are recovered. The difference in the length of the adaptation region and the Re at which canonical properties are recovered are related to the trips employed. Several of these studies thus reflect the necessity for employing appropriate trip designs, for a given flow, in order to ensure the desired boundary layer state is achieved. (Erm and Joubert, 1991; Schlatter and Örlü, 2012).

It is clear from these studies that the trip's configuration (both their shape and size) plays the dominant role in the length of the adaptation region. Another key conclusion is that careful design of the trips (particularly size) is necessary in order to minimize the adaptation region. However, the

influence of the trip's geometry remains unclear. This study aims to provide a more complete and detailed picture of the flow in the vicinity of a selection of representative trips and inform how this relates to the adaptation region. Moreover, it will also aim to understand the flow physics of the beginning of the adaptation region and how distinct flow structures influence its length (the reader is referred to section 4 for a deeper discussion of how different geometries influence the adaptation region). Contrary to the traditional methodology (assessment of the location and velocity needed for a particular trip to recover the canonical properties of the TBL only by far-field measurements); this approach has the advantage of focusing on the predominant flow features near the obstacles and how those flow features influence the behaviour of the TBL in the far field. Recently, Rodríguez-López et al. (2016a,b) (henceforth RBB16 for brevity) associated relatively short adaptation regions with the postulated *wall-driven* mechanism. Longer periods of adaptation (and worse recovery of the TBL canonical properties in general) were associated with the *wake-driven* mechanism. A brief summary of those studies follows:

RBB16 studied the downstream evolution of artificially generated high Re TBL employing two different families of trips. Those trips were, on one hand, high aspect ratio trips (cylinders) and on the other hand low aspect ratio trips (sawtooth fence). Here aspect ratio is defined as the typical wall-normal dimension of the trips divided by their characteristic spanwise length. A deep study involving both one- and two-points simultaneous statistics revealed that the adaptation region downstream of the cylinders was significantly shorter than in the sawtooth fence case, in which the influence of the trips was clearly seen in the last measurement station ($\approx 4\,\mathrm{m} \approx 250$ obstacle heights downstream of the obstacles). Note that the two-point correlations are necessary to reveal the interaction of the outer (wake) fluid with the inner (near-wall) structures. The explanation given by RBB16 is based on the two clearly differentiated mechanisms mentioned above; these are summarized as follows. (i) Cylinders generate a *wall-driven* mechanism; the obstacles leave the inner structures of the boundary layer relatively undisturbed which subsequently drive the mixing of the obstacle's wake with the wall-bounded flow. (ii) the sawtooth fence generates a *wake-driven* mechanism in which the inner structures are more strongly disrupted and once they are re-formed further downstream they do so with an enhanced influence of the obstacle's wake. A similar explanation has also been given by Marusic et al. (2015) who proposes that the obstacle's wake introduces large-scale energetic motions in the intermitent region of the boundary layer which enhances their influence in the near-wall region.

Note that the study conducted by RBB16 only focused on the mid- and far-field development of the TBL and did not consider the flow immediately downstream of the trips. The present study will use high speed Particle Image Velocimetry (PIV) in the vicinity of the trips in order to assess the different mechanisms of formation of the artificially thick TBL. In particular this study will try to define and characterize the source mechanisms that influence the length of the adaptation region from the trips. This result is of primary importance for future researchers who want to carefully design a transition-

tripping device (or an obstacle for artificial generation of high Re TBL). The following results show that indeed the two formation mechanisms are radically different and that this may be the cause of the distinct evolution of the behaviour of the various trips with the downstream coordinate.

The structure of the paper can be summarized as follows: Section 2 describes the trip geometry and the experimental set-up. Section 3 presents the PIV results for the current geometries and their subsequent analysis using Optimal Mode Decomposition, and assessing the influence of the flow field and the turbulent/non-turbulent interface in the near-wall region. Section 4 discusses whether the two mechanisms described in the paper can be extrapolated to other geometries, and how they can explain some of the differences appearing in the literature. Finally, section 5 draws the conclusions of the study.

2 Experimental methodology

2.1 The wind tunnel

Experiments were conducted in the 18 inch closed-circuit wind tunnel at Imperial College London. This experimental facility has a square test section $457 \times 457 \,\mathrm{mm}^2$ (width $\times$ height) with parallel walls. The background turbulence intensity is 0.15% at the freestream velocity used in the present study $U_\infty \approx 11 \,\mathrm{m/s}$. A 12 mm thick perspex flat plate, 1.2 m long, is mounted horizontally at mid height spanning the whole test section with the leading edge located 300 mm downstream of the beginning of the test section. A 10 : 1 aspect ratio elliptic leading edge followed immediately by a 20 mm long strip of sand paper are mounted to the flat plate to mimic the configuration employed by RBB16. The freestream velocity is kept constant using a PID controller which reads the flow speed from a Pitot-static tube located in the freestream, upstream of the flat plate. Two different spanwise distributed arrays of trips are employed representative of the two distinct behaviours characterized by RBB16; their geometrical parameters are described in Table 1. These trips were located in a machined slot 160 mm from the leading edge, spanning 89% of the test section. The coordinate origin is located in the centre plane with x as the downstream coordinate, y the wall-normal coordinate and z the spanwise coordinate. $x = 0$ is placed at the most downstream available position for each trips, that is, the end of the second row of cylinders for *2row20* and the tip of the sawtooth fence for *Saw*. Note that this coordinate definition varies slightly with that presented in RBB16 where the coordinates were measured from the leading edge of the plate, in particular their most upstream measurement point was located at 0.446 m which, in the current coordinate system, is equivalent to $x \approx 270 \,\mathrm{mm}$. A sketch of the experimental set-up is shown in figure 1. Throughout the paper the total velocity in the streamwise direction ($U = u + u'$) is decomposed in the mean (u) and fluctuations (u'). Analogously $V = v + v'$ for the wall-normal velocity. The only component of the vorticity that can be calculated is the spanwise, $\Omega\mathbf{k} = (\omega + \omega')\mathbf{k}$, where $\mathbf{k}$ is the unit vector in the spanwise (z) direction. The sub-script rms is used to denote the root mean square
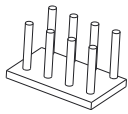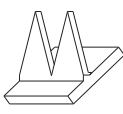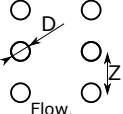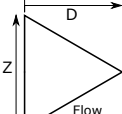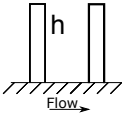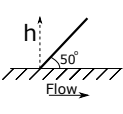
	2row20	Saw	2row20			Saw	
Symbol	★	▽					
h (mm)	20	15.3					
D (mm)	3	12.8					
Z (mm)	10	20					
			Kornilov and Boiko (2012)			Sargison et al. (2004)	

Table 1: Trips' description. Three dimensional sketches are shown for each trip geometry along with their plan and side views.

of the fluctuations of any quantity. Throughout the paper quantities normalized with the obstacle height and/or the freestream velocity will be designed by the superscript $\wedge$, e.g. $\hat{x} = x/h$, $\hat{u} = u/U_\infty$.

2.2 Particle Image Velocimetry

High speed particle image velocimetry (PIV) is conducted in two wall-normal/streamwise $(x - y)$ planes downstream of each trip configuration (one behind the obstacle and another behind the gap between them). Illumination is provided by a Litron LDY300 laser; a spherical lens of focal length 1000 mm and a cylindrical lens of focal length -4 mm are employed to obtain a laser sheet of $\lesssim 1$ mm of thickness. Special attention was paid to ensure that the field of view was located 1 m after the spherical lens in order to make the thickness of the laser sheet as small as possible ($\lesssim 1$ mm). Two 4 Megapixel Phantom v641 cameras are mounted side by side as shown in figure 1 with 105 mm $f/8$ Nikon lenses. The 2560×1600 sensor is cropped to 2560×800 in order to be able to increase both the sampling frequency ($f_s = 1431$ Hz) and time ($T = 3.8$ s). Afterwards the vector fields are stitched together taking a weighted average of both frames in the overlap region to provide a smooth transition. Two campaigns of 5471 images each were acquired for each configuration in order to improve the statistical convergence of the results. This sampling time is approximately equivalent to 2800 shedding cycles in the *2row20* case. The acquisition was made in double frame mode with a time separation between frames of $\Delta t = 25\,\mu$s. This time separation was found to be a compromise between precision in the high speed regions and the capacity to resolve the strongly turbulent region immediately downstream of the trips.

The seeding employed was made of a water-glycol $(4:1)$ solution, the average particle diameter was $d = 2 - 3\,\mu$m and the Stokes number

$$Stk = \frac{t_0}{t_f} = 0.10\,, \quad t_0 = \frac{\rho_{seed} d^2}{18\mu} = 1.92 \cdot 10^{-5}\,\text{s}\,, \tag{1}$$

where $\rho_{seed} = 1025\,\text{kg/m}^3$ is the density of the seeding solution, μ is the air viscosity, and $t_f = \tilde{\Delta}x/U_0$
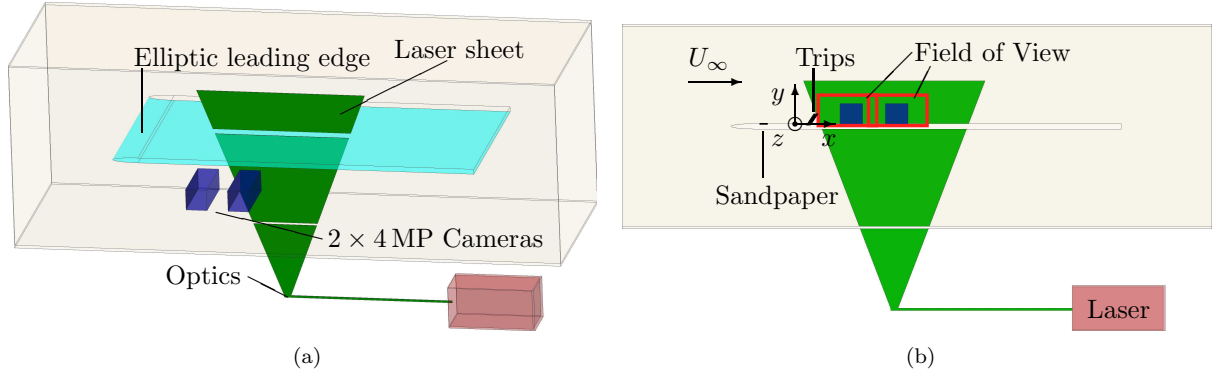
Figure 1: Three dimensional (a) and side (b) views of the experimental arrangement for the PIV experiment. Flow is going from left to right.

is the minimum time scale of the fluid. This is taken as the ratio between the minimum scale that the PIV window can resolve, i.e. the PIV resolution: $\tilde{\Delta}y = \tilde{\Delta}x = 0.95\,$mm, and the mean velocity at the closest point from the wall, where the smallest eddies are assumed to be located, $U_0 = 5\,$m/s. In these conditions the Stokes number is $Stk < 1$ in the near-wall region; in regions further from the wall, the typical length scale is expected to be larger than this value hence this estimation of Stk is in that respect a conservative approach.

The images are preprocessed subtracting the background luminosity and normalizing the particle intensity to the local background level in order to account for non-uniformities in the illumination. The quantisation dynamic range of the images was never lower than 7 bits. After the preprocessing a recursive processing is conducted with an initial window size of $48 \times 48\,$px and a final interrogation region size of 16×16px with a 50% overlap. The resulting vectors were rejected if the peak ratio of the correlation was smaller than 1.3 and the deviation with respect of the 8 nearest neighbours was larger than 3 times the local spatial standard deviation. Groups with less than 6 vectors were not considered, in any case, the rejected vectors were always fewer than 1%.

This set-up provided a spatial resolution of $\tilde{\Delta}x = \tilde{\Delta}y = 0.95\,$mm equal in the streamwise and wall-normal directions; and a vector spacing $\Delta x = \Delta y = 0.47\,$mm. Due to reflections from the flat plate and the local high shear the first row of vectors at $y_0 = 0.47\,$mm was not available for every downstream position, therefore it was discarded and results are presented with the first velocity measurement at $y_0 = 0.95\,$mm. The field of view was approximately $250 \times 40\,$mm in the (x, y) coordinates respectively. This allows a qualitative comparison between the results at the end of this domain ($x = 250\,$mm) with the first measurement point in RBB16 ($x \approx 270\,$mm). In particular, using the value of the friction velocity $u_\tau = \sqrt{\tau_{wall}/\rho}$ given in RBB16 for that point one can estimate that the closest velocity measurement to the wall is at $y_0^+ = y_0 u_\tau/\nu > 20$ and the resolution is $\tilde{\Delta}x \approx \mathcal{O}(20\,\nu/u_\tau)$ where τ_{wall} is the shear stress at the wall, and ρ is the air density. Hence extrapolation of the shear stress from the velocity profile is not possible in the present experiment (Rodríguez-López et al., 2015; Örlü et al., 2010).
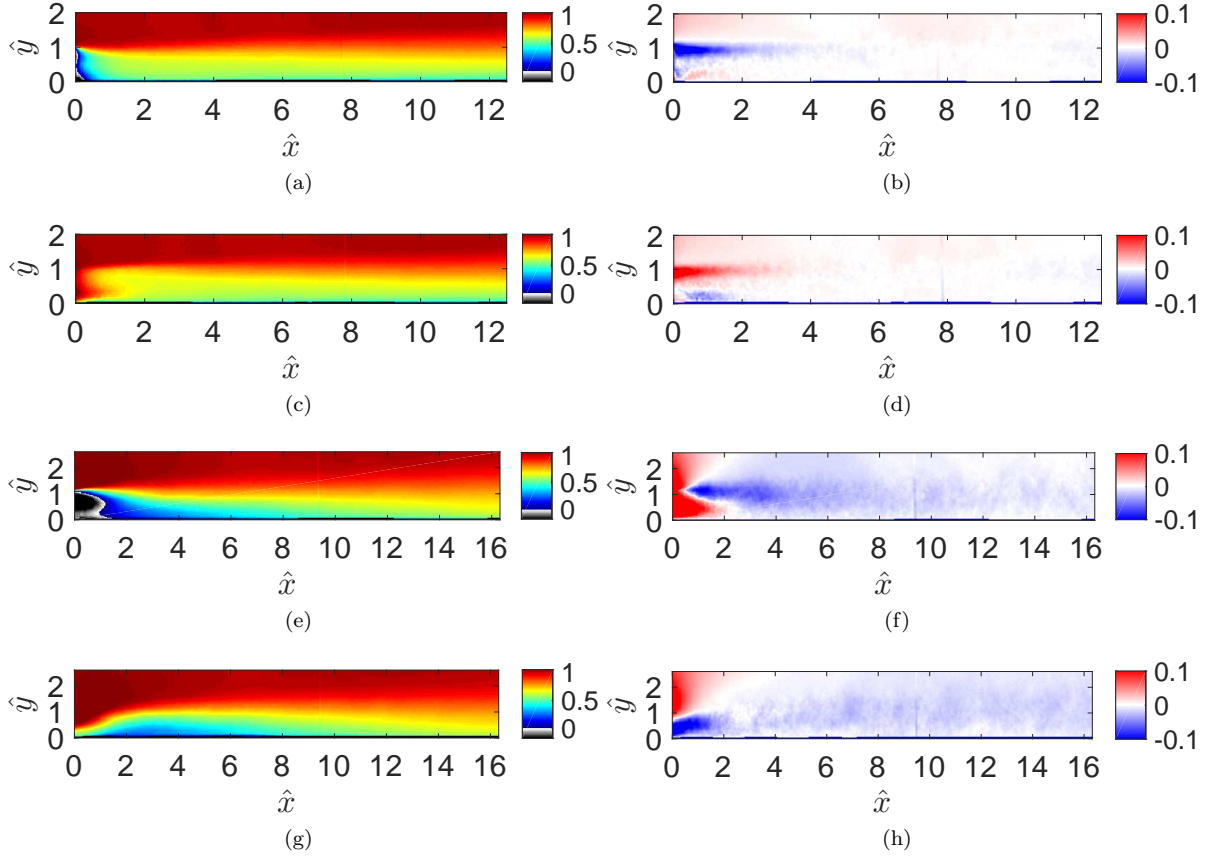
Figure 2: (a,c,e,g) Streamwise, $\hat{u}$, and (b,d,f,h) wall-normal, $\hat{v}$ mean velocity contours for (a-d) *2row20* and (e-h) *Saw* trips behind an obstacle (a,b,e,f) and behind a gap (c,d,g,h). The gray-scale part of the colormap denotes negative streamwise velocity.

3   Results

The main aim of this section is to present a full characterization of the flow field in the vicinity of the trips in order to assess which are the main features that give rise to the distinct behaviours for the two trips employed. After showing averaged results of the flow field, a reduced order model of the flow is shown in section 3.3 extracting the main dynamically significant features. Later on, the flow close to the turbulent/non-turbulent interface (section 3.4) and the near-wall region (section 3.5) are presented. These results allow to understand all the phenomena involved in the flow in the close vicinity of the trips. Finally, the sketch presented in figure 11 include the main findings of the study and summarizes the most important flow features.

3.1   Mean quantities

Two PIV planes were used for each trip configuration, one of them behind the obstacle (that is, behind a cylinder for the *2row20* case, and coincident with the tip of the sawtooth fence in the *Saw* case) and one in the gap. As expected, the flow is initially highly inhomogeneous, due to the spanwise periodic distribution of jets and wakes, and tends to homogenize by the end of the field of view. The mean

velocities are shown in figure 2 where one can see the predominant features of each configuration. In particular, notice the large recirculation region after the *Saw* trip which is only present downstream of the obstacle. This recirculation region disappears after ≈ 1.5 obstacle heights due to its mixing with the jet-like behaviour from its sides. With respect to the *2row20* case, the spanwise combination of jet-like and wake-like behaviour is also present but without a significant recirculation region. Comparison of figures 2(b) and 2(d) shows that the most remarkable feature is the change in vertical velocity close after the tip of the cylinder; this is highly negative after the obstacle (due to vortices with negative spanwise vorticity being detached from their tip) and positive in the gap between two cylinders (due to the deviation of the fluid particles above the cylinder array). The intensity of these phenomena is significantly reduced by $\hat{x} = 3 \leftrightarrow 20$ diameters downstream of the trips.

As seen in figure 2 the most characteristic features of both *gap* and *obstacle* configurations are attenuated for $\hat{x} \approx 6$. Even after this point the flow remains inhomogeneous in the spanwise direction, but the differences are quantitatively smaller in magnitude. Figure 3 gives an illustration of the spanwise recovery of the streamwise velocity (both mean and rms) for the most downstream measurement location ($x \approx 250\,\mathrm{mm} \leftrightarrow \hat{x}|_{2row20} \approx 12, \hat{x}|_{Saw} \approx 16$) for both the *2row20* and *Saw* cases. Despite the slightly poorer collapse of the rms profiles (which may also be attributed to a poorer statistical convergence), this result suggests that only small quantitative differences may appear at the end of the domain but no qualitative changes are expected. For this reason, and in order to keep the clarity and length of the study within reasonable limits, the following results will only be presented for the field of view aligned with the obstacle.

The turbulent fluctuations are higher for the *Saw* trip than for the *2row20* case for every y (figure 3(b)); in particular, there is a qualitative difference in the near-wall region. for $y \to 0$ in the *2row20* case the turbulent fluctuations tend to increase (As corresponds to a TBL in which the maximum of the fluctuations is in the buffer region, $y^+ = 15$). However, this trend is not followed by the *Saw* trips where, based on spectral hot-wire measurements (figure 9, $x = 0.446\,\mathrm{m}$, RBB16), the fluctuations are sufficiently high in the turbulent core as to affect the near wall region.

In order to identify the most active areas of the flow field one can compute the production of turbulent kinetic energy. Due to the high shear that the wall imposes, it seems reasonable to assume that the derivatives of the mean flow in the wall-normal direction will be much higher than those in the stream- or span-wise directions (at least after a small region near the trips). With regards to the spanwise velocity, $w = \partial w/\partial x = \partial w/\partial y = 0$, due to symmetry. However, the terms $\overline{u'w'}\partial u/\partial z$, $\overline{v'w'}\partial v/\partial z$ and $\overline{w'^2}\partial w/\partial z$ are not null in principle, but w' cannot be obtained with planar PIV for the present experiment. Given that the strongest spanwise inhomogeneities are located very close to the trips (c.f. figure 2); it seems reasonable to assume that their effect would be restricted to a small region close to the trips and neglecting these terms would not affect the subsequent study. Under these assumptions
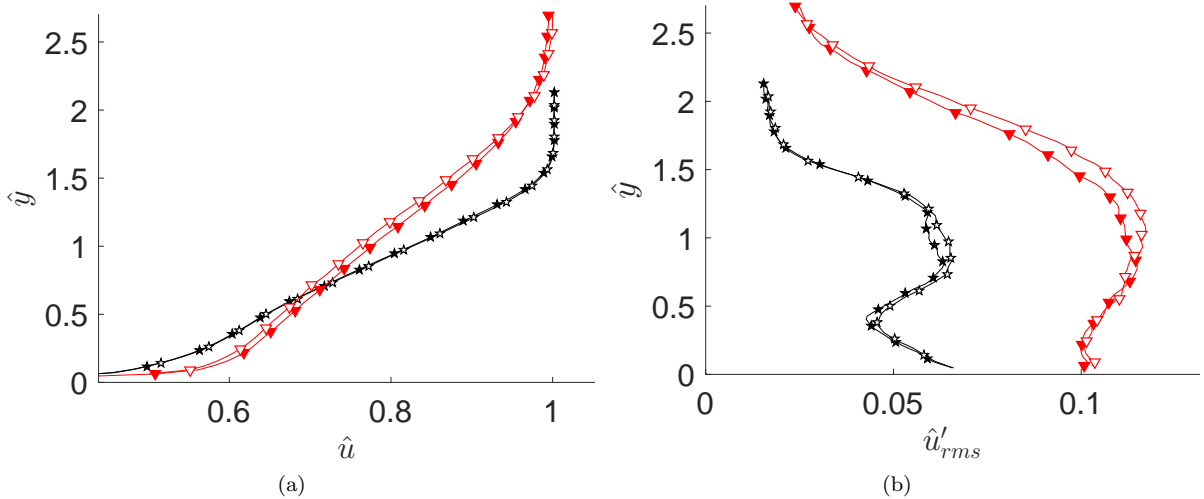
Figure 3: (a) Mean, $\hat{u}$, and (b) root mean square, $\hat{u}'_{rms}$, velocity profiles of streamwise velocity at the end of the field of view ($x \approx 250$ mm). Symbols are given in table 1 (*2row20*= $\star$, *Saw*=$\triangledown$). Empty and filled symbols represent measurements taken downstream of a gap or an obstacle respectively

and limitations the turbulent production can be written as

$$\hat{\mathcal{P}} = \frac{h}{U_\infty^3} \left[-\overline{u'v'}\frac{\partial u}{\partial y} - \overline{v'^2}\frac{\partial v}{\partial y} - \overline{u'^2}\frac{\partial u}{\partial x} \right] . \tag{2}$$

Figures 4(a) and 4(b) show the contours of turbulent production in the flow field calculated acording to equation 2 whereas figures 4(c) and 4(d) show only the contribution of the first term of equation 2. As can be seen, the main contributor to the production is the first term, except in a very confined region close to the trips where the streamwise gradients are larger due to the recirculations. The vertical stripes present at $\hat{x} \approx 8$ are due to a reflection of the laser illumination which are enhanced due to the streamwise derivation and should not be wrongly attributed to a physical mechanism.

Two different behaviours are clearly discernible for the two distinct trips. On the one hand, the high production region for the *2row20* case is concentrated in a narrow strip immediately downstream of the obstacle's tip and it remains at a virtually constant height over the whole field of view; in particular note that this region of high turbulent kinetic energy production is never close to the wall. In contrast, the *Saw* obstacles generate a region of considerably higher production (up to 5 times stronger) which, for $3 < \hat{x} < 7$, extends to very close to the wall. This is in agreement with the spectral behaviour previously reported (c.f. figure 9, $x = 0.446$ m, RBB16) in which the energy in the wake of *2row20* trips is restricted to a very thin region in the vicinity of their tip. With respect to the magnitude of $\hat{\mathcal{P}}$. Note also, as mentioned, that production is significantly higher overall for the *Saw* case than for *2row20*.

In order to study how the two geometries of obstacles influence the future development and growth of the artificially generated TBL one should focus on those parts of the fluid which will be responsible for driving both growth and behaviour of the TBL. RBB16 proposed that two clearly distinct mechanisms were responsible for the different far-field behaviours encountered. The main difference between those
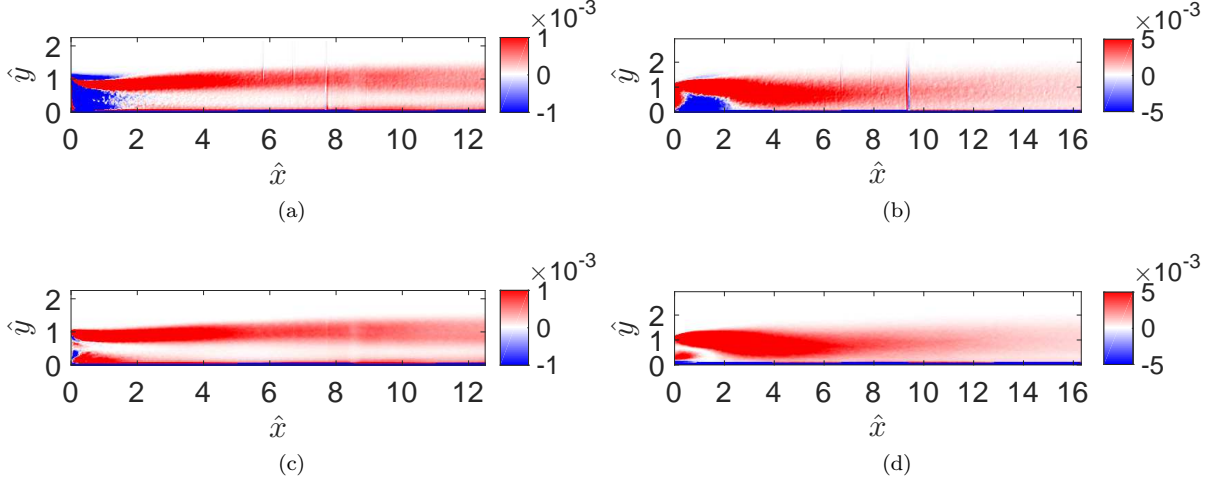
9

Figure 4: Contours of turbulence production, $\hat{\mathcal{P}}$, (first row; a,b); and $\frac{h}{U_\infty^3}\left[-\overline{u'v'}\frac{\partial u}{\partial y}\right]$ component (second row; c,d). For *2row20* (a,c) and *Saw* (b,d) trips behind an obstacle. Note the change in colour scale for the different tripping conditions.

mechanisms is the influence of the relatively high speed fluid of the detached wake and the freestream into the wall regions. This influence is reported to be highly significant in the *wake-driven* mechanism while it remains negligible for the *wall-driven* case. Moreover, the growth rate of a TBL is dominated by the conversion of freestream fluid into turbulent. Hence, the way in which the outer part of the wake behaves and, in particular, the conversion of the freestream into turbulent fluid at the turbulent/non-turbulent interface will partly determine the far field behaviour of the flow. The next section will characterize and study the behaviour of this interface and how its properties influence and explain the various features mentioned above.

3.2 Geometry of The Turbulent/Non-Turbulent Interface

The turbulent/non-turbulent interface (henceforth, TNTI for brevity) is defined as the thin layer of fluid which bounds the turbulent region and outside of which the fluid is non-turbulent (e.g. Corrsin and Kistler 1955). This region has been extensively studied in different flows such as jets (e.g. Westerweel et al. 2005), boundary layers (e.g. Ishihara et al. 2015) or free shear flows (e.g. da Silva et al. 2014). In order to define it, the methodology consists of defining a quantity which changes rapidly from the turbulent to the non-turbulent part of the fluid and establishing a threshold to distinguish both zones. In most cases (including those cited above) this quantity is enstrophy which, in the turbulent core (neglecting the contribution of small pockets of irrotational fluid which may be engulfed) is non-zero and is close to zero in the freestream. However, this method presents difficulties in the current experiment, namely, the highly turbulent and out of plane motions in the vicinity of the trips established a constraint in the time delay between frames of the PIV. This fact, together with the background turbulence of the wind tunnel, generates spurious spanwise vorticity fluctuations due to experimental noise. Hence,
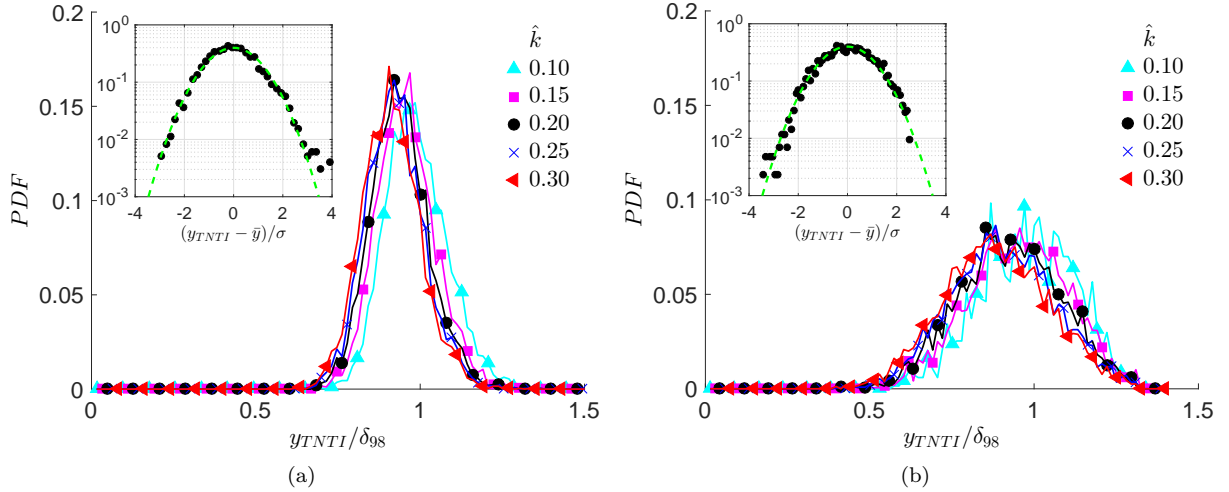
Figure 5: Probability density function, PDF, of the TNTI height at $x \approx 250\,mm$ for *2row20* (a) and *Saw* (b) trips and different threshold values, $\hat{k} = \{0.1, 0.15, 0.2, 0.25, 0.3\}$. Note that some markers are removed to improve the clarity of the plot. Inset shows only the $\hat{k} = 0.2$ value along with a Gaussian distribution (the dashed green line) of the same mean and standard deviation.

it could not be used as the discriminant magnitude for the TNTI detection. Recently, Chauhan et al. (2014) proposed using a pseudo turbulent kinetic energy, $\hat{k}$, to detect the TNTI:

$$\hat{k} = 100 \frac{1}{9U_\infty^2} \sum_{m,n=-1}^{1} \left[(U - U_\infty)^2 + (V)^2 \right] , \tag{3}$$

where m and n represent the sum over a 3×3 grid centred on each point. This magnitude should be close to zero in the freestream (equivalent to the background turbulence of the wind tunnel) and increase rapidly in turbulent parts of the flow. To select an appropriate threshold, an iterative process was followed; a value small enough has to be chosen in order to detect all the turbulent fluid, but it cannot be too small since the noise of the freestream would be detected as turbulence. Chauhan et al. (2014) use a value of $\hat{k} = 0.12$ but also report how it may be necessary to choose a different value for each experiment. In the present case, various thresholds were used in the range $0.1 \leq \hat{k} \leq 0.3$. For each set of images the following process was followed:

- Select a threshold value $\hat{k} = \{0.1, 0.15, 0.2, 0.25, 0.3\}$ and detect which regions of the fluid are turbulent or not.

- For each snapshot take only the longest continuous TNTI; i.e. remove the small *islands* of non-turbulent fluid inside the turbulent region and vice-versa.

- Given the high tortuosity of the TNTI this can appear as multivalued (more than one value for a given x); in this case, only the lower value is taken in order to ensure that all the fluid detected as turbulent is indeed turbulent (the results did not change qualitatively if the upper envelope was used).
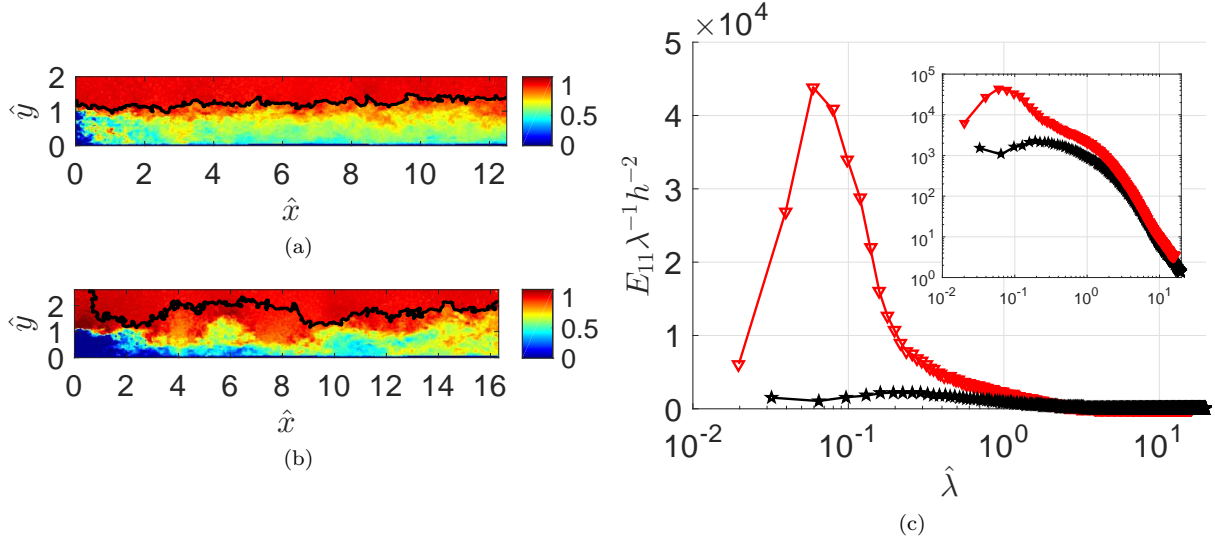
Figure 6: (a,b) Arbitrary snapshot of streamwise, $\hat{u}$ velocity contours for *2row20* (*a*) and *Saw* (*b*) trips. The black solid line shows the instantaneous contour of the TNTI. (c) Spatial normalized pre-multiplied power spectral density of the TNTI height for *2row20* ($\star$) and *Saw* ($\triangledown$) trips.

- In about 10% of the vector fields, because of the high variance in the wall-normal location of the TNTI, this does not cross the field of view left to right but it is interrupted on the upper edge (specially in the *Saw* case due to its larger fluctuations). These vector fields are discarded in order to ensure that the TNTI is a continuous line for the whole field of view. The bias introduced in the statistics because of this is not expected to significantly affect the drawn conclusions. These extreme events are at a large distance from the wall whilst the primary focus of this study is the influence caused by outer fluid on the near-wall behaviour. We are thus more concerned with events in which the TNTI is instantaneously located close to the wall, which are captured with our experimental setup.

- The probability density function, PDF, of the height of the TNTI is plotted at different downstream positions in order to check the threshold sensitivity.

Figure 5 shows the PDF of the TNTI height at a downstream location close to the end of the field of view. The boundary layer thickness, δ_{98}, considered as the height at with the mean velocity profile reaches $0.98U_{\infty}$, is employed as normalization parameter for the TNTI height. With respect to the different thresholds, it is easy to distinguish that the smallest $\hat{k} = 0.1$ presents a different behaviour; a slight deviation from the asymptotic trend is also seen for $\hat{k} = 0.15$. However, for higher values of the threshold, $\hat{k} = \{0.2, 0.25, 0.3\}$, the results are virtually independent of the chosen value. Hence the selected threshold value is the smallest possible inside those of uniform behaviour. Given the small sensitivity to the value of the threshold a finer tuning of its value was not necessary and $\hat{k} = 0.2$ is used for the subsequent analysis. In the inset of figure 5 the PDF is compared with a Gaussian trend for $\hat{k} = 0.2$. As can be seen, there is a good overall agreement so it can be concluded that the height of the

12

TNTI follows a normal distribution. The slight deviations on the tails may be due to poor convergence at very low probabilities; note also that the right tail for the *Saw* case does not have any measurement since the field of view was not sufficiently large in the y-extent to capture the most extreme events of the TNTI.

There are two further results that present a difference between the *2row20* and *Saw* trips: first, it is easy to see that there is a significantly lower deviation, σ, in the position of the TNTI for the *2row20* case than for the *Saw* case. This effect may be consistent with the presence of recirculating flow which generates large rolling motions downstream of the *Saw* trip. Second, one can consider the tortuosity, θ, of the curves. Defining s as the longitudinal coordinate along the path of the TNTI allows us to define the tortuosity as the longitudinal coordinate per unit of downstream distance ($\theta = s/\Delta x$). The value of this relation is significantly different in the *Saw* case and in the *2row20* case, $\theta_{Saw} = 2.50 > \theta_{2row20} = 1.69$. Hence *Saw* trips generate a longer and more wrinkled TNTI with a higher variation in position. Examples of an instantaneous TNTI plotted over streamwise velocity contours are shown in figures 6(a) and 6(b) displaying the aforementioned characteristics. Furthermore, in order to study the cause of the difference in the characteristic length (tortuosity) of the TNTI, one can study its spatial spectrum. Figure 6(c) shows the normalized pre-multiplied power spectral density of the height of the TNTI, $E_{11}(y_{TNTI}(s))\lambda^{-1}h^{-2}$, where $\hat{\lambda} = \lambda h$ is the wave number non-dimensionalized with the obstacle height. Note that the spectra is calculated considering $y_{TNTI}(s)$ where s is the longitudinal coordinate following the interface. This result shows that the origin of the different tortuosity comes from an increased prevalence of long wave lengths. Despite a similar behaviour for small scales, the energy content for scales larger than $5h$ is approximately 10 times greater for the *Saw* trips than for the *2row20* case.

Recent studies suggest that, in the vicinity of the TNTI, the conversion of non-rotational fluid into turbulent happens at a small scale, nibbling (Corrsin and Kistler, 1955), whereas the large scale motions (traditionally known as engulfment) contribute to increase the area in which the nibbling occurs (see for instance: da Silva and Taveira, 2010; Westerweel et al., 2005; da Silva et al., 2014; Chauhan et al., 2014, amongst others). The previous results would therefore suggest that for the *Saw* case there is a greater contribution to the overall entrainment through large-scale engulfment, whereas the small-scale nibbling behaviour seems to be more similar in both cases.

To summarize: On the one hand *2row20* generate a less wrinkled TNTI which, despite being located closer to the wall on average ($\bar{y}/\delta_{98}|_{2row20} < \bar{y}/\delta_{98}|_{Saw}$), has a low deviation from its mean position. On the other hand *Saw* trips generate a longer TNTI for the same downstream distance with a significantly greater energy content for larger scales. Its mean position is further from the wall but with a high variance which makes its minimum position much closer to the wall than its counterpart. These results, in particular, the different energy content at large scales in the TNTI, suggests that the flow field can

be simplified by means of a low order modelling method which enables a decomposition into the most dynamically significant modes. This decomposition can be seen as a dynamical filter which will allow us to understand why the large scales have one order of magnitude more energy in the *Saw* case than in the *2row20* case and, more specifically, what is the role of the large rolling motions hypothesised above in the *Saw* case.

3.3 Optimal Mode Decomposition

Given the complexity of the flow under consideration, modal reduction methods are potential candidates to generate a low order model of the flow field which can be studied. One of the most widespread methods for low order modelling is Proper Orthogonal Decomposition, POD, (Berkooz et al., 1993). In this technique, various orthogonal modes are selected and ranked according to the kinetic energy they contain. A significant disadvantage of this method when applied to the present problem, is the lack of use of dynamical information contained in the time resolved PIV. In order to solve this problem, recently Schmid (2010); Schmid et al. (2011) developed the Dynamical Mode Decomposition, DMD, a method in which, taking as the primary basis the aforementioned POD modes, one can also introduce the dynamically relevant information of the flow. This advance made it possible to detect fluid structures with a low kinetic energy but high dynamic significance, which, in the POD case, would have been hidden by other fluid phenomena less dynamically important but more energetic. More recently, Wynn et al. (2013) developed a generalization of the aforementioned method (Optimal Mode Decomposition, OMD) in which the modes are not specified *a priori*. This new method conducts an optimization process in order to select the modes which best represent the dynamical processes involved. This method has been successfully applied to flows in which, small, less energetic flow structures' modes are successfully identified in a multi-scale flow (Baj et al., 2015). A brief summary of the method follows; for further explanations and a deeper mathematical analysis the reader is referred to Wynn et al. (2013).

Let $\mathbf{UV}_j \in \mathbb{R}^{2N_{xy}}$ be the vector field of the snapshot $j = 1 \ldots N$, where N_{xy} is the number of vectors in a given PIV snapshot and N is the number of snapshots in the experiment. The OMD method generates a low order linear model for the temporal evolution $\mathbf{UV}_j \to \mathbf{UV}_{j+1}$ such that $\mathbf{UV}_j = A\mathbf{UV}_{j+1}$. In particular, the OMD method allows us to prescribe r, the rank of matrix A in such way that $A = LML^T$ where $L \in \mathbb{R}^{r \times 2N_{xy}}$, $M \in \mathbb{R}^{r \times r}$ and $\text{rank}(M) = r$. Hence, M can be decomposed into r eigenvalues, Λ, and eigenvectors, P resulting in $A = LP\Lambda P^{-1}L^T$. The OMD solutions are the matrices $\{L, P, \Lambda\}$ that minimize the residual $\sum_{j=1}^{N} ||\mathbf{UV}_j - LP\Lambda P^{-1}L^T \mathbf{UV}_{j+1}||$ subject to $L^T L = I_{r \times r}$. One can define r OMD modes, Φ_i with $i = 1 \ldots r$ as the columns of $\Phi = LP \in \mathbb{R}^{2N_{xy} \times r}$. Furthermore, one can project the snapshot $\mathbf{UV}_j$ onto the mode Φ_i in order to obtain the coefficients $a_j^i \in \mathbb{C}$; thus the OMD reconstruction
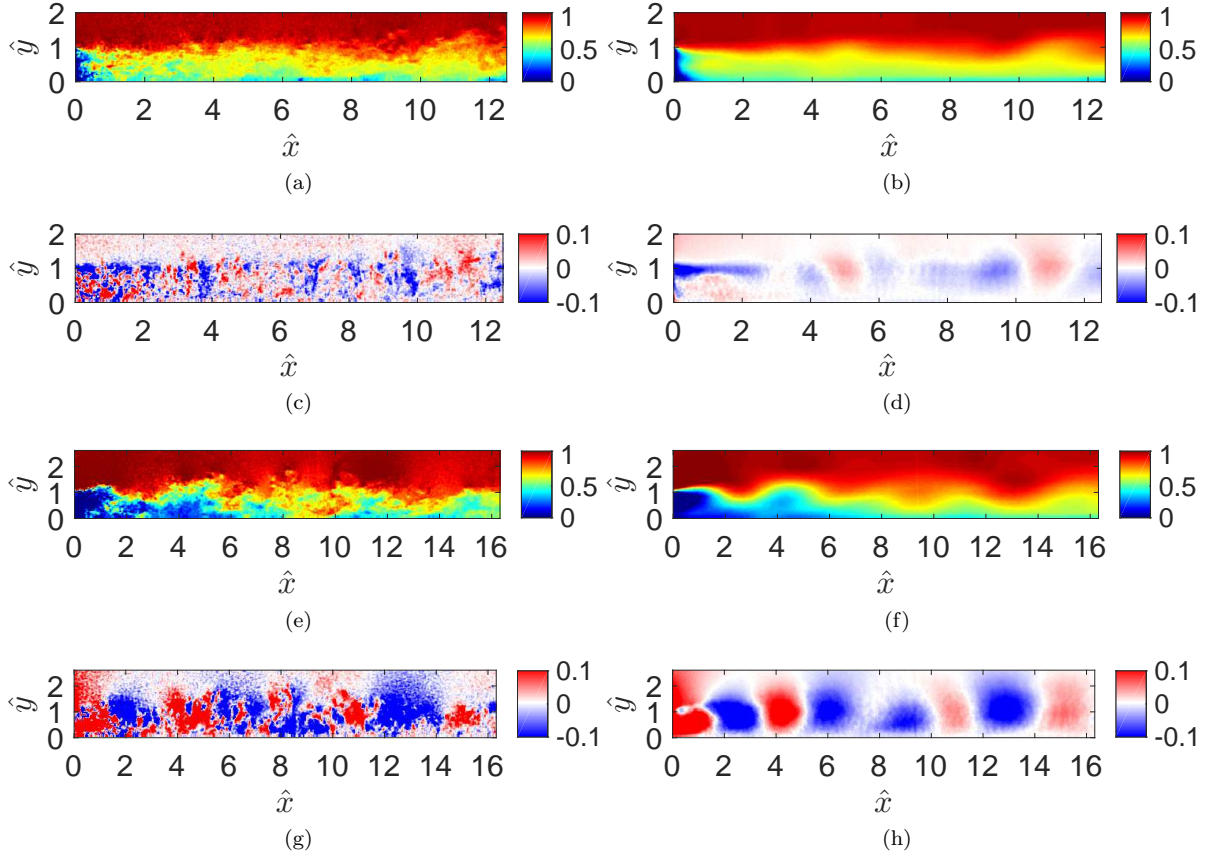
Figure 7: Arbitrary snapshot of (a,b,e,f) streamwise, $\hat{U}$, and (c,d,g,h) wall-normal, $\hat{V}$ instantaneous velocity contours for *2row20* $(a-d)$ and *Saw* $(e-h)$ trips. Raw velocity field (first column, a,c,e,g) and OMD reconstruction with $r = k = 20$ (second column b,d,f,h). See also supplementary material provided for an animated reconstruction of the flow field.

is:

$$\mathbf{UV_j^{rec}} = \sum_{i=1}^{k} a_j^i \Phi_i \,. \tag{4}$$

Note that in general $k \leq r$. The smaller the value of k the more information that is lost in the reconstruction because of not considering the modes $k < i \leq r$. However, given the strong non-linearities of the flow it is important to notice that even in the case $k = r$, $\mathbf{UV}_j^{rec} \neq \mathbf{UV}_j$. Considering λ_i, the eigenvalues of the matrix M, $\text{Re}(\lambda_i)$ is the damping of the i-th mode (the least damped mode is understood as the most dynamically significant) and $\text{Im}(\lambda_i)$ is its characteristic frequency.

Figure 7 shows the original and the reconstructed U and V field using OMD for $r = k = 20$ modes and for both trips employed. The analysis of the reconstructed fields shows that the low order linear model is able to capture the most representative large-scale motions. The differences between the original and reconstructed field are mainly concentrated in the small scales, since this is there where the non-linearities are stronger. In fact, the reconstruction using OMD can be seen as a smart filter in which the velocities are not filtered in relation to their size (or time scale) but, on the contrary, considering their dynamic relevance to the flow. See also supplementary material provided for an animated reconstruction of the

15

flow field available in `http://www.multisolve.eu/OMD/OMD_reconstruction_LowRes_Slow.mp4`.

The least damped mode for the *Saw* case corresponds to the recirculation downstream of the obstacle. In the *2row20* case, three out of the four least damped modes are associated with the tip vortices; that is, they remain confined at a height similar to the obstacle height not interacting with the near-wall region. This contrasts with the most relevant modes for the *Saw* case which show dynamically representative fluid structures at heights very close to the wall. This feature can be also seen in the reconstructed vertical velocity field; on it, one can appreciate two mean characteristic features for each trip. First, the magnitude of the reconstructed vertical velocity is significantly higher in the *Saw* case than in *2row20*; second, the coherent structures are closer to the wall contrasting with the *2row20* where they are confined in the tip vortex region. These facts provide the first evidence of the two mechanisms proposed by RBB16 in which the highly energetic wake generated by the *Saw* case strongly influences the wall region by the so called *wake-driven* mechanism. Analysing the structures' sizes confirms that the origin of the larger energy contained in longer wave lengths of the TNTI (discussed in section 3.2) is associated with the recirculation and the large rolling motions. Moreover, the information extracted from the modes shows that the most important mode is the recirculation, which suggests that this wake driven mechanism may not be exclusive to this particular geometry but in fact may just be associated with any obstacle shape which generates a significant recirculation and strong vertical motion able to enhance the influence of the outer layer in the inner region of the forming boundary layer. This possibility is discussed at length below in section 4.

3.4 Flow field in the vicinity of the TNTI

Once the most dynamically significant flow features have been spotted in sections 3.1, 4.1 and 3.3 above; this section will characterize the flow in the immediate vicinity of the TNTI. Although the larger wavelength shapes present in the TNTI are significantly more energetic for the *Saw* case in comparison with *2row20* trips (by an order of magnitude), there is not such a difference in the small wavelengths. Therefore, the flow field in the vicinity of the TNTI will be studied more closely, in order to explore the different mechanisms present at the interface. To do so, conditional averages of various parameters can be calculated in the region near the interface. Let us define ξ as the local coordinate of the TNTI in such a way that $\xi = 0$ at the TNTI and the freestream is the region $\xi > 0$. Note that this local coordinate is defined parallel to the wall-normal axis, y, and not normal to the local TNTI. The average of an arbitrary quantity ϕ conditioned to the position of the TNTI will be represented as $< \phi >$.

Figure 8 shows the conditional average of the streamwise velocity component, $< \hat{u} >$, and the spanwise vorticity component, $< \hat{\omega} >$, plotted against ξ/δ_{98}. The mean velocity in the vicinity of the interface presents a structure in which two different slopes can be distinguished; a linear decay of velocity in the fully turbulent core followed by a steeper change across the interface. A possible definition of the
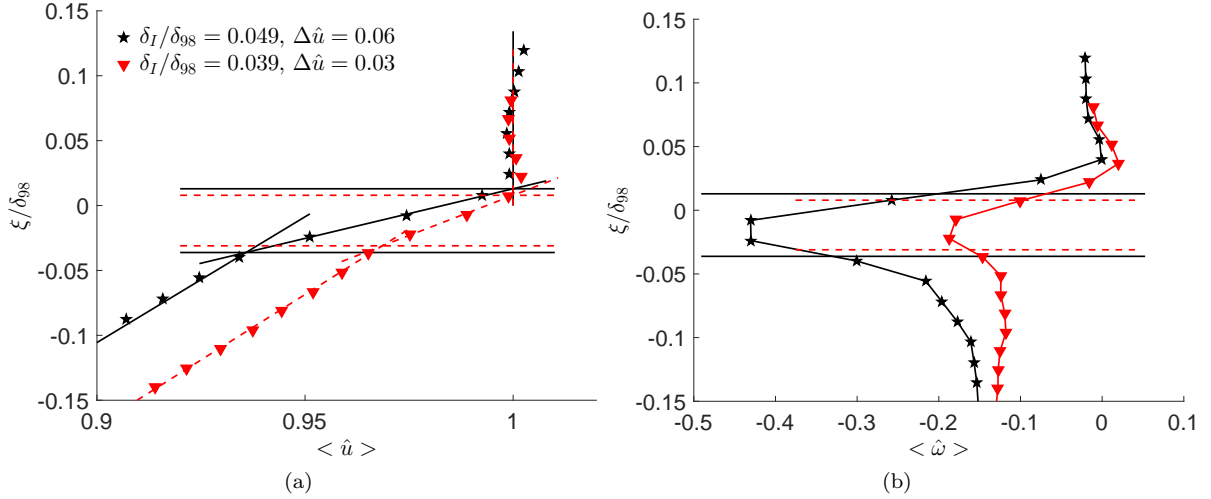
Figure 8: Conditional average of streamwise velocity $< \hat{u} >$, (a) and spanwise vorticity, $< \hat{\omega} >$, (b) across the TNTI (located at $\xi = 0$). Symbols are given in table 1. (*2row20* $= \star$, *Saw* $= \triangledown$).

interface thickness, δ_I, is the region of the flow in which this steeper change in $< \hat{u} >$ occurs (Chauhan et al., 2014). This thickness definition is shown in figure 8(a) along with the linear trends fitted to the conditional averaged velocity profile. Note that the same lines are highlighted in figure 8(b) and there is an agreement between this definition of interface thickness and the peak in the conditional average of the spanwise vorticity. This observed *jump* in streamwise velocity has been reported previously in TBLs (Chauhan et al., 2014) and jets (Westerweel et al., 2005); defining $\Delta \hat{u}$ as its magnitude allows us to quantify the difference in behaviour for both trips. Although the thickness of both interfaces is virtually the same, the *Saw* case produces a less sharp rise $\Delta \hat{u} = 0.03$ compared with $\Delta \hat{u} = 0.06$ for the *2row20* case. The same physics are evident in the vorticity plot where the peak vorticity for the *2row20* case is almost double that of the *Saw* case. A brief explanation for these behaviours may be the small but with a strong spanwise vorticity vortices detached from the tip of the cylinders contrasting with the larger vortices which enhance the vertical homogenization of the flow for the *Saw* case (c.f. right part of figure 11).

In order to further study how the different-size eddies influence the turbulence fluctuations in the TNTI vicinity, one can consider the correlations across the interface defined as:

$$\rho_{uu}(\xi_1, \xi_2) = \frac{\int_0^\infty u'(\xi_1, t)u'(\xi_2, t)\mathrm{d}t}{u'_{rms}(\xi_1)u'_{rms}(\xi_2)} \ . \tag{5}$$

Figure 9 shows the correlation curves of streamwise velocity fluctuations originated right above the interface. In particular, the distance that the correlation of the fluctuations requires to vanish into the turbulent core is highlighted , δ_ρ. In other words, δ_ρ is a measure of how deep the fluctuations originated right above the TNTI can penetrate into the turbulent core. In contrast to the previous definition of thickness based on the streamwise velocity jump ($\delta_I/\delta_{98}|_{Saw} \approx \delta_I/\delta_{98}|_{2row20}$), δ_ρ yields a distinct value

for both trips $\delta_\rho/\delta_{98}|_{Saw} \approx 0.2 > \delta_\rho/\delta_{98}|_{2row20} \approx 0.05$. This result supports the vortex model proposed above (sketched in the right hand side of figure 11): Sections 3.1 and 3.3 have shown that the *Saw* obstacles generate large vortices, originating from the recirculation region, which increase the transfer of energy between the upper and lower parts of the wall-bounded flow. Since $\omega_z < 0$ for these structures, in the vicinity of the freestream, they induce mainly positive streamwise velocity which has the same direction as the freestream. These relatively large coherent structures increase the distance across which the fluctuations originating in the freestream are correlated. They also reduce the jump in velocity and the peak in vorticity in the TNTI's vicinity. In essence, these large structures increase the correlation length and the transfer of energy between upper and lower parts of the wall bounded flow by inducing a wall-normal velocity (c.f. figure 2). Contrastingly, *2row20* trips generate very energetic tip vortices which remain at a fixed height, far above from the wall (figure 5). These vortices (significantly smaller and with an important spanwise component of vorticity c.f. figure 8(b)) are probably generated by the flow locally being deflected over the tip of the cylinder, as opposed to the main mechanism of vortex shedding along the body of the cylinders. The presence of these small, but highly energetic, vortices induces a very rapid mixing of the non-turbulent fluid into the turbulent area generating a higher velocity jump (figure 8(a)) but sheltering the fluctuations originating in the freestream in a very short distance (figure 9). This rapid loss in correlation has also been reported across turbulent interfaces (Ishihara et al., 2015) and internal shear layers (Ishihara et al., 2013) through the mechanism of shear sheltering.
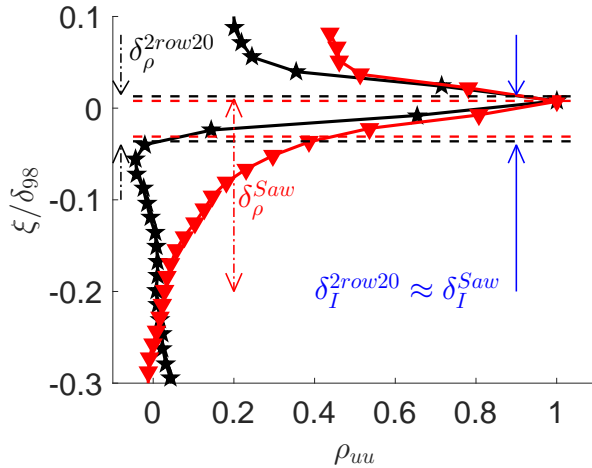

Figure 9: Conditional correlation of streamwise velocity fluctuations $\rho_{uu} = f(\xi)$. Symbols are given in table 1. (*2row20*= $\star$, *Saw*=$\triangledown$). Dashed line shows the thickness of the TNTI based on the velocity jump as defined in figure 8(a). Dot-dashed lines show the approximate length at which the correlation of the fluctuations in the interface vanishes (δ_ρ).

Summarizing the differences in the TNTI behaviour of both trips: (i) *2row20* trips generate smaller, very energetic vortices in the vicinity of the TNTI which generate a sharper velocity jump across the interface in a shorter $\delta_\rho \approx \delta_I$ distance. These vortices are also the origin of the small fluctuation in the height of the TNTI. On the other hand (ii) *Saw* trips generate large recirculating-like coherent motions (c.f. section 3.3 and figure 6(c)) which increase the influence of the outer region in the lower part of the wall bounded flow but generate a smoother transition near the TNTI due to induction of velocity parallel to the freestream. In this case the conversion of freestream fluid into turbulent is more associated

with the engulfment of larger bulges than in the former case. They also generate a significantly higher oscillation of the TNTI position. These main features are summarized in the right hand side of the sketch in figure 11 where the main vortices are depicted along with their assumed behaviour near the TNTI.

3.5 Wall and wake regions

Two important observations: firstly, the TNTI in the *2row20* case is sharper (more clearly delimited) than the *Saw* case and, although being slightly closer to the wall in mean, its variance is significantly smaller. Secondly, *Saw* generates large coherent vortices (due to its recirculation, as shown by the OMD reconstruction), which play a crucial role enhancing the transport of highly energetic fluid from the freestream to the wall region. This section aims to answer how the two distinct regions influence the near-wall region and the growth of the artificially thick TBL generated downstream.

In a naturally growing TBL, over a smooth surface without a pressure gradient, the momentum is only lost at the wall. Hence, near-wall behaviour (with scales u_τ and $\delta_\nu = \nu/u_\tau$) is responsible for driving the far-field characteristics of a wall-bounded flow. The final goal of an artificially generated boundary layer is to obtain a thicker TBL for a given dowsntream distance without changing the canonical properties. Despite the size increase being given by the drag of the obstacles, the far-field development has to be driven by the near-wall region as in the undisrupted case (Although this seems to be clearer for low Re, there is still an open debate whether this is applicable to an asymptotically high Re TBL, see for instance Hunt and Morrison 2000, amongst others). Thus it is of primary importance to study how the near-wall region is influenced by the outer energetic motions detached from the trips. Here the adjective energetic is used to refer to both a higher mean velocity and a higher turbulent activity than the characteristic mean and fluctuating velocities in the near-wall region.

The closest available point to the wall in the present experiment is located at $y_0 = 0.95\,\mathrm{mm} \approx 20\delta_\nu$ for the last position of the field of view ($x \approx 250\,\mathrm{mm}$). This point is considered close enough to the wall so as to be representative of the inner behaviour of the TBL. Although the estimation of the position of the first point in viscous units may have a large uncertainty (particularly in the most disrupted *Saw* case), it is undoubtedly within the overlap layer and hence it is safe to assume that it is characteristic of the inner motions of the TBL (Rodríguez-López et al., 2016a).

In order to assess the influence that external motions have on the near-wall region one can define the correlation of the fluctuations in the near-wall region with those in the wake region as:

$$\rho_{uu}^{wall}(x, y_0, \Delta x, \Delta y) = \frac{\int_0^\infty u'(x, y_0, t)u'(x + \Delta x, y_0 + \Delta y, t)\mathrm{d}t}{u'_{rms}(x, y_0)u'_{rms}(x + \Delta x, y_0 + \Delta y)}. \tag{6}$$

This correlation coefficient depends on the location of the near-wall point chosen, (x, y_0), which is then correlated with the entire flow field. Assuming that the flow field is $(x, y) \in [0, 250] \times [y_0, 40]\,\mathrm{mm}$, the
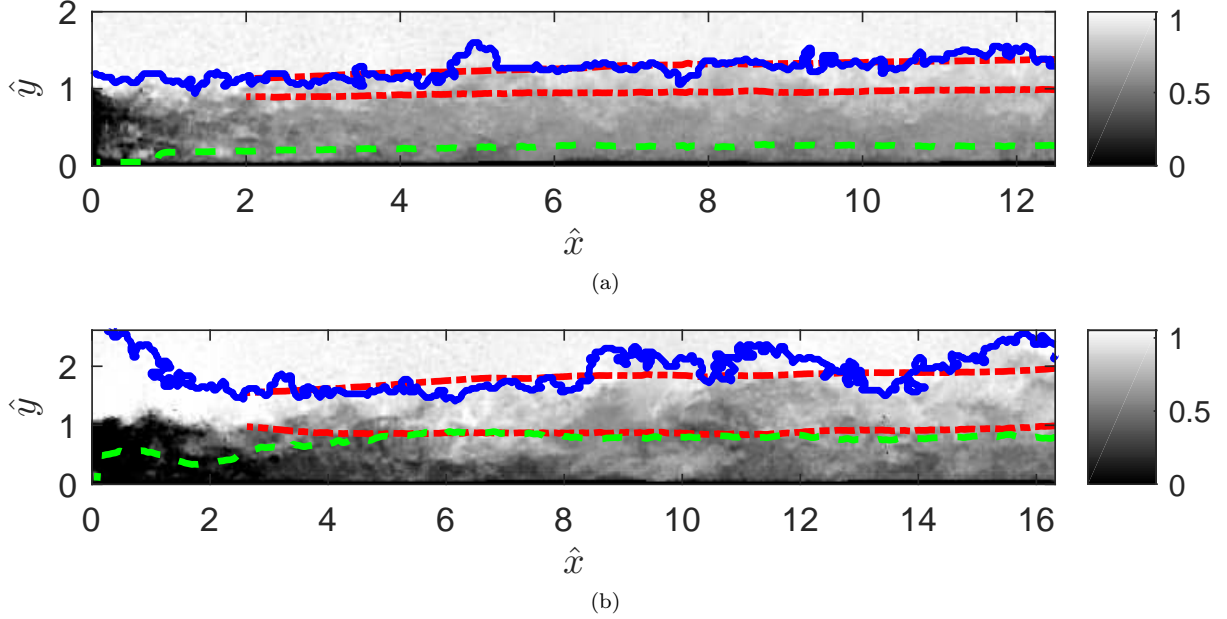
Figure 10: Wall and wake regions for *2row20* (a) and *Saw* (b) shown over an example of streamwise velocity contour. Solid line (blue) shows the instantaneous TNTI. The dashed green line shows the envelope of points with a correlation level from the wall $\rho_{uu}^\star$. The dashed-dotted red lines show the mean, $\bar{y}$, (higher) and minimum, $\bar{y} - 3\sigma$, (lower) positions of the TNTI.

upper and lower bounds for the floating probe are $0 \leq x + \Delta x \leq 250$ mm and $y_0 \leq y_0 + \Delta y \leq 40$ mm for the downstream and wall-normal coordinates respectively. For a given near-wall point, located at an arbitrary downstream position, (x, y_0), one can define a contour around it of a certain correlation level, $\rho_{uu}^\star$. The region within this contour would have a correlation level higher than $\rho_{uu}^\star$ and *vice-versa*. As a first approach one can think that this contour is a unique line, more or less convex, which surrounds the near-wall point selected. For this to be true, one needs to select a high enough value of $\rho_{uu}^\star$ so as to avoid fluctuations about zero correlation for relatively long distances, but small enough to capture all the regions of the flow which are correlated. After a trial and error process, the selected value is $\rho_{uu}^\star = 0.3$ which gives a good compromise between maintaining the correlated region unique around (x, y_0) and capturing all the correlated parts of the flow. In any case the results do not change qualitatively when varying $\rho_{uu}^\star$ due to its low sensitivity.

Repeating this process for every $x \in [0, 250]$ mm and taking the envelope curve of all the single contours around each wall-point provides the curve $y^\star(x)$ which is the upper bound of the region of the flow with a correlation with any point in the near-wall region bigger than the threshold value $\rho_{uu}^\star$. Let us call the part of the flow bounded by $0 < y < y^\star(x)$ as the *Wall region* in order to reflect that it is only in this region where the fluctuations are correlated with the near-wall behaviour.

Section 3.2 allows us to easily define the intermittent region of the flow as the part where the intermittency, γ (estimated by the cumulative density function of the TNTI vertical position, y_{TNTI}) is $0 < \gamma < 1$. Given the Gaussian behaviour of y_{TNTI}, its integral can be represented by the er-
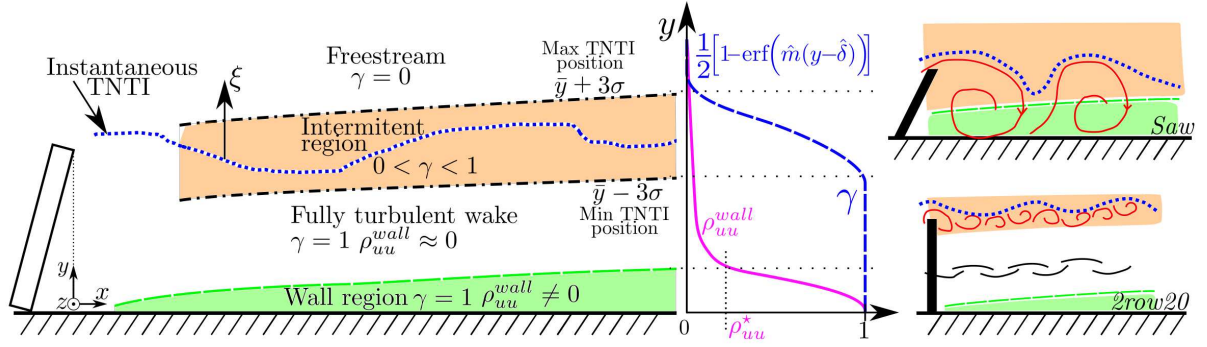
Figure 11: Left part: Sketch of the different regions of the flow distinguishing (from the wall upwards): wall region ($\gamma = 1$, $\rho_{uu}^{wall} \neq 0$), fully turbulent wake ($\gamma = 1$, $\rho_{uu}^{wall} \approx 0$) and intermittent region ($0 < \gamma < 1$). Central part: trend followed by the wall correlation, ρ_{uu}^{wall}, (solid line) and the intermittency, γ, (dashed line). Right part: sketch of characteristic eddies for *Saw* (top) and *2row20* (bottom) trips. Note that there is no fully turbulent wake region in *Saw* case.

ror function as first stated by Klebanoff (1954); and the expression of the intermittency profile results $\gamma = [1 - \mathrm{erf}(\hat{m}(y - \hat{\delta}))]/2$, where $\hat{m}$ and $\hat{\delta}$ can be obtained from a fit to the data. The values for the different trips at $x \approx 250\,\mathrm{mm}$ are $\hat{m}_{Saw} = 0.11$, $\hat{m}_{2row20} = 0.25$, $\hat{\delta}_{Saw} = 31.8$ and $\hat{\delta}_{2row20} = 28.0$. Analogously one can estimate the intermittent region as $\bar{y} - 3\sigma < y < \bar{y} + 3\sigma$ where, as defined above, $\bar{y}$ and σ are the mean and standard deviation of the position of the TNTI at a given downstream location.

In general the intermittent and wall regions are not related so for a sufficiently tall obstacle there is a region in between which is fully turbulent (its intermittency function is $\gamma = 1$) but it is not correlated with the wall ($\rho_{uu}^{wall} < \rho_{uu}^{\star}$). This part of the flow field will be called the fully turbulent wake to distinguish it from the intermittent part and to show that, in this case, it is generated by the obstacle's wake. For a naturally growing TBL this region is also expected to appear for a certain wall-normal extent.

A qualitative sketch of the flow structure is shown in the left hand side of figure 11. In it, the three zones are distinguishable, starting from the wall: Wall region ($0 < y < y^{\star}(x)$ and $\rho_{uu}^{wall} > \rho_{uu}^{\star}$), fully turbulent wake ($\gamma = 1$ and $\rho_{uu}^{wall} \approx 0$), intermittent region ($0 < \gamma < 1$ hence $\bar{y} - 3\sigma < y < \bar{y} + 3\sigma$) and finally the freestream where $\gamma = 0$.

Figure 10 shows these regions for the two different trips. It is strikingly clear that in the *Saw* case the wall region is significantly higher than in the *2row20* case. This fact; together with the large variation of the TNTI position, which indicates that the outer fluid penetrates considerably deeper into the flow field, makes it impossible to define the fully turbulent wake region. The main conclusion that can be drawn from this result for the *Saw* case is that the whole wake detached from the obstacles significantly influences the wall region. Moreover, there are some occurrences of the freestream being engulfed by the large scale motions detached from the trips and brought close enough to the wall so as to directly influence the near-wall region (c.f. supplementary material available in `http://www.multisolve.eu/OMD/OMD_reconstruction_LowRes_Slow.mp4`). This effect is not present in the *2row20* case where the TNTI, despite being closer to the wall on average, remains at a given height over the wall without

influencing the wall region. In the *2row20* case the fully turbulent wake region acts as a damping area that prevents the outer highly energetic fluid from influencing the wall motions. Also this fully turbulent wake region has a lower mean velocity than the freestream and a higher turbulence intensity, hence, the growth of the wall region is favoured by its mixing with this turbulent fluid. Note that, using the same definition and threshold, for a canonical TBL the wall region is confined to $y < 0.15\delta$ (c.f. figure 10b from RBB16) and the minimum position of the TNTI is 0.4δ (c.f. Klebanoff, 1954; Chauhan et al., 2014, amongst others). Thus generating a three layer structure as in the *2row20* case.

Further downstream, the strong tip vortices in the intermittent region diminish their energy and they are also mixed with the near wall region. It generates a TBL with increased thickness but in which the history of the flow has been driven primarily by the wall region. Thus this result describes the *wall-driven* mechanism, first proposed by RBB16, in which the TBL grows from the wall without influence of the outer energetic motions. In contrast, the *wake-driven* mechanism, present for the *Saw* trip, involves large-scale energetic eddies which originate in the recirculation and generate strong vertical motions that strongly influence the wall region disrupting its natural growth and making it considerably more difficult for the artificial TBL to recover the canonical properties (RBB16).

4   Discussion

Section 3 above has presented evidence for the two proposed mechanisms, namely *wake-* and *wall-driven*. There are still two further considerations that can be usefully added to the discussion and will be considered in this section. In the first place it appears the question of whether these proposed mechanisms are exclusive to the particular geometry tested or whether these behaviours can be assumed for other geometries. Secondly, a discussion follows of whether this theory can explain, to some extent, certain results and trends that have appeared previously in the literature.

4.1   Geometrical dependence

An important point, in order to further validate the present study, is to establish whether or not the particular chosen geometry plays an important role in the two mechanisms proposed, and hence determine whether similar mechanisms may be observed for trips with other geometries. This section will present certain reasonable assumptions, according to which, some of the results in the literature can be explained in terms of the two mechanisms proposed in this study. The two main characteristics of the flow fields are the large recirculation-like coherent structures detached from the trips in the *Saw* case; and the ordered horizontal flow without transfer of energetic fluid from the freestream and TNTI to the near-wall region in the *2row20* case. Note also that the OMD reconstruction in section 3.3 has shown that the recirculation and the strong vertical velocities responsible for the enhanced wake interaction in the

near-wall region are linked. This fact suggests that the main characteristic to minimize in order to avoid the *wake-driven* mechanism is the presence of recirculating fluid downstream of the trips. There are several geometrical parameters that can be tuned in order to avoid or generate the recirculation region and these are not exclusive to the present geometries. It seems reasonable to assume that the asymptotic case of the *wake-driven* mechanism is a wall-mounted fence in which all the fluid is deflected over the obstacle thus generating strong recirculating coherent structures with spanwise vorticity.
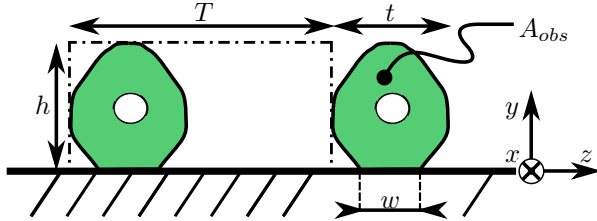

Figure 12: Frontal view of an arbitrary periodic trip geometry in which the following parameters can be defined: $AR = h/t$, $\sigma_{wall} = w/T$, $\sigma_{obs} = A_{obs}/(Th)$.

As a first approach, there are three main geometrical parameters to consider that will determine the formation mechanism: The blockage at the wall, $\sigma_{wall} = w/T$, the blockage of the obstacle, $\sigma_{obs} = A_{obs}/(Th)$, calculated as its frontal area divided by the area of the smallest frame that can surround the obstacle, and the aspect ratio, $AR = h/t$, defined, in the most conservative way, as the ratio between the maximal dimensions in the wall-normal and spanwise directions (see figure 12 for the definition of the parameters). The effect of σ_{wall} modulates how much fluid is deflected over the obstacle to then impinge on the wall region. In the asymptotic case of the wall mounted fence and in the present *Saw* case this is $\sigma_{wall} = 1$. The effect of the blockage (in porous like fences or in wall-mounted obstacles) regulates how much fluid can pass through the obstacle array generating the ordered motions typical from the *wall-driven* mechanism rather than the large recirculation-like vortices typical of *wake-driven* mechanism. In the limiting case of the wall mounted fence, $\sigma_{obs} = 1$ and in the *Saw* and *2row20* cases it is 0.5 and 0.3 respectively. For porous obstacles, the smaller the blockage the weaker the recirculation-like motions would be, since they would be pushed downstream. For medium blockages the aspect ratio also plays an important role; high AR trips, such as wall mounted cylinders shed vortices with a wall normal axis which minimizes the interaction between the upper and lower parts of the wake, contrary to low aspect ratio trips in which the direct impingement of the turbulent structures enhance this interaction. The limiting case of the wall mounted fence has $AR \to 0$. *Saw* and *2row20* trips have aspect ratio of 0.77 and 6.7 respectively.

From this reasoning, it can be deduced that in order to avoid the *wake-driven* mechanism one can decrease the blockage of the trips and increase their aspect ratio to avoid recirculation over the trip and avoid total blockage at the wall. In any case, intermediate configurations, such as a spanwise array of wall mounted cubes ($AR = 1$, $\sigma_{obs} = 0.3$) would have an intermediate behaviour. It is reasonable to expect in that case that a recirculation over the obstacles would exist but the parallel flow between two cubes would partly dilute this recirculation confining and reducing its effect. Thus it seems reasonable

23

to postulate that the different mechanisms can be explained from the various flow features involved and they may not be exclusive to the tested geometries. However, establishing clear borders in the behaviour for the different parameters involved is not easy and should be considered independently for such intermediate cases.

4.2 Revisiting some literature

Some of the different behaviours documented in the literature can be explained assuming that the two described formation mechanisms are responsible for them. A few of these examples are discussed below.

One of the first examples in the literature considering the exhaustive study of boundary layer thickening devices followed by an adaptation region and a recovery of canonical properties was Klebanoff and Diehl (1951) who used rods, a fine mesh grid and sand roughness. Amongst the trips employed they reported that the rods were rapidly discarded due to their extraordinarily long adaptation region. They also reported the great sensitivity to any disturbances of the mean profile which was also confirmed later by Chauhan et al. (2009) and Marusic et al. (2015) testing up to the 10th order moment. Klebanoff and Diehl (1951) concluded that a trip should remove energy from the freestream without introducing large scale disturbances. This intuitive observation is confirmed here and described as the *wake-driven* mechanism, in which the large scale disturbances play the main role due to the enhanced influence that the outer region has on the lower part of the TBL. We may also consider the study of Marusic et al. (2015) along the same lines, who deliberately overstimulated the TBL in order to obtain a gain in thickness. The trips employed were two threaded rods, horizontally placed, of different diameters. In this case, the adaptation region is maintained up to ≈ 2000 trip heights downstream of the obstacles; amongst the longest adaptation region of any reported in the literature. This may also be explained by the extreme case studied in which the geometry is the limiting case for the *wake-driven* mechanism as described above.

As mentioned in the introduction, the study by Castillo and Johansson (2002), claiming that the canonical properties will not be recovered until $Re_\theta = 5000$, seems in contradiction with the value proposed by Schlatter and Örlü (2012) of $Re_\theta = 2000$. This discrepancy may be attributed to the wire employed as a trip by Castillo and Johansson (2002) which was relatively large in size (and presumably also large with respect to the thickness of the undisturbed boundary layer at the trip location, although this value is not mentioned in the study). In other words, the trip employed appears to give rise to the *wake-driven* mechanism which is assumed to have the longest recovery length. As such, this adaptation region could have been shortened through the use of a trip which avoids such a mechanism.

Another relevant example is Kornilov and Boiko (2012), who employed a spanwise distributed array of vertical cylinders and assessed the validity of the turbulent boundary layer with (amongst others) the Clauser equilibrium parameter $G = \sqrt{2/C_f}(H-1)/H$. Here $C_f = 2u_\tau^2/U_\infty^2$ is the friction coefficient and

H is the shape factor (the ratio of displacement to momentum thickness). In this study, they determined that the canonical properties were recovered after a certain adaptation region which was a function of the height of the trips. Later, Kornilov and Boiko (2013) presented a similar study but this time with a grid of horizontal rods; they reported that the canonical properties of the TBL were not recovered at any downstream position measured. Analysing both geometries one can infer that this may be due to the change from *wall-* to *wake-driven* mechanism when swapping from vertical to horizontal rods due to their different mechanism of shedding.

Okamoto (1986, 1987) studied the evolution of a boundary layer downstream of various wall-mounted plates finding that, in terms of the recovery of canonical properties, the worst configuration was a solid wall mounted fence (purely *wake-driven*); followed by square plates with $AR = 1$ and $\sigma_{obs} = 0.5$ (an intermediate behaviour). Finally he concluded that the best recovery of the canonical properties was obtained using wall-mounted triangular plates normal to the flow with $AR = 2$ and $\sigma_{obs} = 0.25$. This was the only trip amongst the ones he used in which the flow field may be associated with the *wall-driven* mechanism.

Two further studies in which there are no trips involved are Alving and Fernholz (1996) and Castro and Epik (1998) who studied the boundary layer formed downstream of a recirculation bubble. This recirculation was generated by an adverse pressure and a blunt trailing edge respectively. Both of them conclude that the recovery of canonical properties is slow (meaning a longer adaptation region) and that the outer fluid presents an extraordinary high influence in the development of the near-wall turbulence. Similarly to the present study, Alving and Fernholz (1996) concluded that the relaxation process is controlled by the outer energetic motions (*wake-driven*) in a way that it is not *usually seen* in canonical boundary layers, whose growth can be described by the *wall-driven* mechanism.

5 Conclusions

The study of PIV data in the near field of two classes of wall-mounted trips has revealed two distinct formation mechanisms for the TBL growing downstream of them. These two mechanisms were first hypothesized by RBB16 who associated them with the differences in length for the adaptation region downstream of the trips. This region is defined as the downstream length required to recover the canonical properties of the TBL, where no influence of the trips remains present. The properties of the two mechanisms are described as follows:

The *Wall-driven* mechanism is generated by a spanwise array of wall-normal cylinders whose dominant shed vortices are dominated by wall-normal vorticity. These trips only generate weak vertical motions confined at a constant height about the tip region. The TNTI generated is thinner and it is characterized by a larger velocity jump across it. Although closer to the wall on average than its counterpart, its

deviation from the mean position is significantly lower. These facts reduce the influence of the high speed fluid on the near-wall region to a minimum and allow us to differentiate three zones from the wall upwards: The near-wall region, the fully turbulent wake, in which fluctuations are not correlated with the wall and the intermittent region. This mechanism is associated with shorter lengths of the adaptation region. Under reasonable assumptions this mechanism may also be attributed to low-blockage high aspect ratio trips.

The *Wake-driven* mechanism is found in a spanwise wall-mounted sawtooth fence; in this case, the most characteristic feature is the strong recirculation downstream of the trips which generate significant vertical motions, increasing the transfer of information between the outer part of the wake and the near-wall region. Another important feature is the distance of the fluid structures to the wall, which is much smaller than the former case. In this case, the TNTI is characterized by a smaller jump of velocity across it and a larger thickness based on the conditional correlation. A greater deviation from the mean position is also found implying that the influence of the high speed fluid in the near-wall region is substantially greater. Contrary to the previous case, only two zones can be distinguished since the whole wake of the trips is correlated with the near-wall fluctuations; hence one cannot define a fully turbulent wake region which isolates the near-wall behaviour from the outer fluid. This mechanism is related with very long adaptation regions which present a different eddy structure to that expected in a natural TBL (c.f. RBB16). A review of the existent literature suggests that (i) this mechanism may not be exclusive of this geometry and (ii) a wall-mounted solid fence may be the limit case for this mechanism.

References

Alving, A. E. and Fernholz, H. H. (1996). Turbulence measurements around a mild separation bubble and downstream of reattachment. *J. Fluid Mech.*, 322:297–328.

Arie, M., Kiya, M., Suzuki, Y., and Sakata, I. (1981). Artificial Generation of Thick Turbulent Boundary Layers. *The Japan Society of Mechanical Engineers*, 24(192):956–964.

Armitt, J. and Counihan, J. (1968). The Simulation of the Atmospheric Boundary Layer in a Wind Tunnel. *Atmos. Environ.*, 2(1):49–71.

Baj, P., Bruce, P. J. K., and Buxton, O. R. H. (2015). The triple decomposition of a fluctuating velocity field in a multiscale flow. *Phys. Fluids*, 27(7):075104.

Berkooz, G., Holmes, P., and Lumley, J. L. (1993). The Proper Orthogonal Decomposition in the Analysis of Turbulent Flows. *Ann. Rev. Fluid Mech.*, 25:539–575.

Castillo, L. and Johansson, T. (2002). The effects of the upstream conditions on a low Reynolds number turbulent boundary layer with zero pressure gradient. *J. Turbul*, 3(031):1 – 19.

Castro, I. and Epik, E. (1998). Boundary layer development after a separated region. *J. Fluid Mech.*,

274:91–116.

Chauhan, K., Philip, J., de Silva, C. M., Hutchins, N., and Marusic, I. (2014). The turbulent/non-turbulent interface and entrainment in a boundary layer. *J. Fluid Mech.*, 742:119 – 151.

Chauhan, K. A., Monkewitz, P. A., and Nagib, H. M. (2009). Criteria for assessing experiments in zero pressure gradient boundary layers. *Fluid Dyn. Res.*, 41(2):021404.

Cook, N. (1978). Wind-tunnel simulation of the adiabatic athmopheric boundary layer by roughness, barrier and mixing device methods. *J industrial aerodynamics*, 3(2):157–176.

Corrsin, S. and Kistler, A. L. (1955). Free-stream boundaries of turbulent flows. Technical report, NACA Technical report TN-1244, Washington D.C.

Counihan, J. (1969). An improved method of simulating an atmospheric boundary layer in a wind tunnel. *Atmos. Environ.*, 3(2):197–214.

da Silva, C. B. and Taveira, R. R. (2010). The thickness of the turbulent/nonturbulent interface is equal to the radius of the large vorticity structures near the edge of the shear layer. *Physics of Fluids*, 22(12):121702.

da Silva, C. B., Taveira, R. R., and Borrell, G. (2014). Characteristics of the turbulent/nonturbulent interface in boundary layers, jets and shear-free turbulence. *J. Phys. Conf. Ser.*, 506:012015.

Davidson, M. J., Snyder, W. H., Lawson, R. E., and Hunt, J. C. R. (1996). Wind tunnel simulation of plume dispersion through groups of obstacles. *Atmos. Environ.*, 30(22):3715–3731.

Erm, L. P. and Joubert, P. N. (1991). Low-Reynolds-number turbulent boundary layers. *J. Fluid Mech.*, 230:1–44.

Hunt, J. C. R. and Fernholz, H. (1975). Wind-tunnel simulation of the atmospheric boundary layer: a report on Euromech 50. *J. Fluid Mech.*, 70(3):543.

Hunt, J. C. R. and Morrison, J. F. (2000). Eddy structure in turbulent boundary layers. *European Journal of Mechanics - B/Fluids*, 19(5):673–694.

Ishihara, T., Kaneda, Y., and Hunt, J. C. R. (2013). Thin Shear Layers in High Reynolds Number Turbulence - DNS results. *Flow Turbul Combust*, 91(4):895–929.

Ishihara, T., Ogasawara, H., and Hunt, J. C. (2015). Analysis of conditional statistics obtained near the turbulent/non-turbulent interface of turbulent boundary layers. *J. Fluid Struct.*, 53(February 2015):50–57.

Klebanoff, P. (1954). Characteristics of Turbulence in a Boundary Layer with Zero Pressure Gradient. Technical report, National Advisory Comitee for Aeronautics Report 1247.

Klebanoff, P. and Diehl, Z. (1951). Some Features of Artificially Thickened Fully Developed Turbulent Boundary Layers with Zero Pressure Gradient. Technical report, NACA, Thecnical Note 2475.

Kornilov, V. I. and Boiko, A. V. (2012). Wind-tunnel simulation of thick turbulent boundary layer. *Thermophys and Aeromech*, 19(2):247–258.

Kornilov, V. I. and Boiko, A. V. (2013). Simulation of a thick turbulent boundary layer via a rod grid. *Thermophys and Aeromech*, 20(3):289–302.

Marusic, I., Chauhan, K. A., Kulandaivelu, V., and Hutchins, N. (2015). Evolution of zero-pressure-gradient boundary layers from different tripping conditions. *J. Fluid Mech.*, 783:379–411.

Marusic, I., McKeon, B. J., Monkewitz, P. A., Nagib, H. M., Smits, A. J., and Sreenivasan, K. R. (2010). Wall-bounded turbulent flows at high Reynolds numbers: Recent advances and key issues. *Phys. Fluids*, 22(6):065103.

Nagib, H. M., Morkovin, M. V., Yung, J. T., and Tan-atichat, J. (1976). On Modeling of Atmospheric Surface Layers by the Counter-Jet Technique. *AIAA Journal*, 14(2):185–190.

Okamoto, S. (1986). Turbulent shear flow behind rows of square plates placed on a plane boundary. *Atmos. Environ.*, 20(8):1537–1546.

Okamoto, S. (1987). Turbulent shear flow behind a single row of bluff obstacles placed on plane boundary. *Atmos. Environ.*, 21(6):1295–1303.

Örlü, R., Fransson, J. H. M., and Alfredsson, P. H. (2010). On near wall measurements of wall bounded flows. The necessity of an accurate determination of the wall position. *Prog. Aerosp. Sci.*, 46(8):353–387.

Rodríguez-López, E., Bruce, P. J. K., and Buxton, O. R. H. (2015). A robust post-processing method to determine skin friction in turbulent boundary layers from the velocity profile. *Exp. Fluids*, 56(4):681–16.

Rodríguez-López, E., Bruce, P. J. K., and Buxton, O. R. H. (2016a). Downstream evolution of perturbations in a zero pressure gradient turbulent boundary layer. In *Progress in turbulence VI, Proceedings of the iTi conference in Turbulence 2014.*, 21-24 September 2014, Bertinoro, Italy.

Rodríguez-López, E., Bruce, P. J. K., and Buxton, O. R. H. (2016b). On the formation mechanisms of artificially generated high Reynolds number turbulent boundary layer. *Bound-Lay Meteorol*, (In press. DOI: 10.1007/s10546-016-0139-8).

Sargison, J. E., Walker, G. J., Bond, V., and Chevalier, G. (2004). Experimental review of devices to artificially thicken wind tunnel boundary layers. In *15th Australasian Fluid Mechanics Conference*, number December, 13-17 December, Sidney, Australia.

Schlatter, P. and Örlü, R. (2012). Turbulent boundary layers at moderate Reynolds numbers: inflow length and tripping effects. *J. Fluid Mech.*, 710:5–34.

Schmid, P. J. (2010). Dynamic mode decomposition of numerical and experimental data. *J. Fluid Mech.*, 656:5–28.

Schmid, P. J., Li, L., Juniper, M. P., and Pust, O. (2011). Applications of the dynamic mode decomposition. *Theor Compl Fluid Dyn*, 25(1):249–259.

Westerweel, J., Fukushima, C., Pedersen, J. M., and Hunt, J. C. R. (2005). Mechanics of the turbulent-

nonturbulent interface of a jet. *Phys. Rev. Lett.*, 95(17):1–4.

Wynn, A., Pearson, D. S., Ganapathisubramani, B., and Goulart, P. J. (2013). Optimal mode decomposition for unsteady flows. *J. Fluid Mech.*, 733:473–503.